

Spin and Charge Resolved Quantum Gas Microscopy of Antiferromagnetic Order in Hubbard Chains

Martin Boll^{1*}, Timon A. Hilker^{1*}, Guillaume Salomon^{1*}, Ahmed Omran¹, Immanuel Bloch^{1,2}, and Christian Gross^{1†}

¹*Max-Planck-Institut für Quantenoptik, 85748 Garching, Germany, and*

²*Fakultät für Physik, Ludwig-Maximilians-Universität, 80799 München, Germany*

(Dated: 17 May 2016)

The repulsive Hubbard Hamiltonian is one of the foundational models describing strongly correlated electrons and is believed to capture essential aspects of high temperature superconductivity. Ultracold fermions in optical lattices allow for the simulation of the Hubbard Hamiltonian with a unique control over kinetic energy, interactions and doping. A great challenge is to reach the required low entropy to observe antiferromagnetic spin correlations beyond nearest neighbors, for which quantum gas microscopes are ideal. Here we report on the direct, single-site resolved detection of antiferromagnetic correlations extending up to three sites in spin-1/2 Hubbard chains, which requires an entropy well below $s^* = \ln(2)$. Finally, our simultaneous detection of spin and charge opens the route towards the study of the interplay between magnetic ordering and doping in various dimensions.

The Hubbard model, describing strongly correlated lattice fermions, supports a rich phase diagram at low temperatures. Despite the conceptual simplicity of the Hubbard model, parts of its phase diagram, especially away from half filling, and its connection to high temperature superconductivity are still under debate [1]. Here, controlled experiments with ultracold fermions in optical lattices might provide new insight [2]. For one particle per site, the so called half filling regime of a balanced two component fermion mixture, and repulsive interactions, the Hubbard model features a crossover from a metallic to a Mott insulating state when lowering the temperature. For even lower temperatures, antiferromagnetic correlations are expected to develop in the Mott insulating phase due to the superexchange mechanism [2–5]. The paramagnetic Mott insulating state has been observed in seminal ultracold atom experiments involving trap averaged quantities and, recently, at the single atom level [6–12]. Detailed experimental studies of the thermodynamics of the Hubbard model also revealed its equation of state in the charge sector down to temperatures at which short range ordering might occur [13, 14]. Unfortunately, the experimental preparation of low entropy lattice fermions has turned out to be extremely challenging, making the observation of longer ranged antiferromagnetism difficult. Important progress in revealing magnetic ordering in the Hubbard model has been reported with the observation of nearest neighbor correlations via singlet-triplet spin oscillations [15–17] and short range correlations deduced from optical Bragg spectroscopy [18]. However, the detection of the onset of magnetic order turned out to be challenging because of the inhomogeneity of the trapped samples, in which different phases coexist. Microscopic control or detection

helps to overcome this limitation and the analogue of antiferromagnetic correlations has been measured in small systems of up to three fermions [19]. Recently, local, non spin-resolved detection of ultracold fermions in single lattice sites has been demonstrated [20–23] and the non-uniform entropy distribution in band and Mott insulating states has been observed in the charge sector [11, 12, 24].

Here we report on a site- and spin-resolved study of antiferromagnetic correlations in one-dimensional spin-1/2 Hubbard chains realized with ultracold lithium-6 in an optical superlattice. Using our novel spin and onsite atom number sensitive quantum gas microscope, we directly measure spin correlations together with charge fluctuations in the system. Our measurements reveal finite-range antiferromagnetic Heisenberg correlations extending over up to three sites. Furthermore, we measured the strength of the spin correlations for increasing interactions, consistent with isentropic lattice loading. Finally, we observed the decrease of antiferromagnetic correlations away from half filling and the freezing out of charge fluctuations at low entropy.

The fermionic spin-mixture formed in each of our one-dimensional lattice tubes is well described by the single band Hubbard Hamiltonian

$$\hat{H} = -t \sum_{i,\sigma} (\hat{c}_{i,\sigma}^\dagger \hat{c}_{i+1,\sigma} + \text{h.c.}) + U \sum_i \hat{n}_{i,\uparrow} \hat{n}_{i,\downarrow} + \sum_{i,\sigma} \epsilon_i \hat{n}_{i,\sigma}. \quad (1)$$

Here the fermion creation (annihilation) operator is denoted by $\hat{c}_{i,\sigma}^\dagger$ ($\hat{c}_{i,\sigma}$) at site i for each of the two spin states $\sigma = \uparrow, \downarrow$. The operator $\hat{n}_{i,\sigma} = \hat{c}_{i,\sigma}^\dagger \hat{c}_{i,\sigma}$ counts the number of atoms with spin σ on the respective site. Three competing energy scales govern the physics of this system: intersite nearest-neighbor hopping with strength t , onsite interactions of strength U and local trap induced energy offsets ϵ_i . While t is controlled via the lattice depth, U can be tuned independently in the experiment using the broad Feshbach resonance of lithium-6 between the lowest hyperfine states $|\downarrow\rangle = |F = 1/2, m_F = -1/2\rangle$

* These authors contributed equally to this work.

† Electronic address: christian.gross@mpq.mpg.de

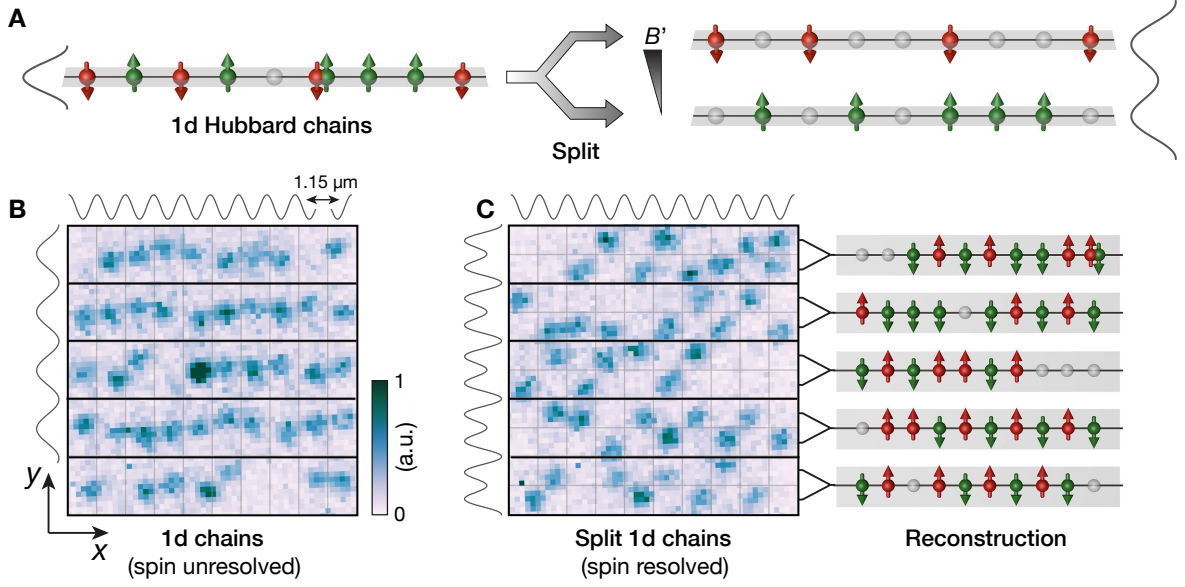


FIG. 1. **Schematic of the spin and charge resolved detection.** (A) Schematic of the spin resolved imaging. Each site of the Hubbard chain was split spin-dependently into a local double well potential. During the splitting process a magnetic field gradient B' was applied to separate the two spins. This allows for the simultaneous detection of $|\uparrow\rangle$ (green), $|\downarrow\rangle$ (red) spins, doublons (red and green spins overlapping) and holes (gray spheres) and thus for a full characterization of the Hubbard chains. (B) Typical fluorescence image of atoms in five mutually independent one-dimensional tubes imaged prior to splitting. The lattice potentials are indicated by the black lines next to the images with a spacing along the tubes oriented in x -direction of $1.15 \mu\text{m}$ and a transverse inter-tube separation of $2.3 \mu\text{m}$. The increasing fluorescence level is shown by darker colors in relative units as represented by the color bar. Our imaging slightly displace the atoms from their original positions and also allows for the detection of doubly occupied sites (saturated signal in the center) [24]. (C) Typical image with spin resolved detection. A superlattice in y -direction (indicated on the left of the image) was used to split each chain in a spin dependent manner. The $|\downarrow\rangle$ spins were pulled down, while the $|\uparrow\rangle$ spins were pulled upwards. The right image illustrates the reconstructed Hubbard chains.

and $|\uparrow\rangle = |1/2, 1/2\rangle$ [25]. In the experiments reported here, we exclusively worked with repulsive interactions $U > 0$, for which the Hubbard model supports finite range antiferromagnetism with correlations suddenly appearing at distances beyond nearest neighbors for entropies per particle below the “critical” value of $s^* = S/Nk_B = \ln(2)$ [26–28]. Importantly, true long range order is absent in the 1d Hubbard model even at zero temperature [4, 29], and the resulting algebraic decay of the correlations is significant even on a distance of a few sites [27, 28]. In the limit of very strong repulsive interactions and half-filling, the emerging spin order is intuitively understood from the mapping of the Hubbard model to a Heisenberg antiferromagnet with superexchange coupling $J = 4t^2/U$ [3]. For lower interactions, particle-hole fluctuations become important and the ground state is characterized by a spin density wave with reduced correlations in the spin sector [5]. In one dimension, the model is Bethe ansatz integrable [4, 29] and precise predictions for the finite entropy spin correlations and charge fluctuations have been reported in the relevant parameter regime of cold atom based experiments [27, 28].

Our experiments started with the preparation of a low

temperature balanced spin mixture of the $|\uparrow\rangle$ and $|\downarrow\rangle$ states in a single two dimensional lattice plane [24]. The final temperature and atom number was controlled by magnetic field driven spill-out evaporation at repulsive interactions [30]. We set the final interaction strength using a homogeneous magnetic offset field to control the scattering length in the vicinity of the Feshbach resonance centered at 832 G [25]. Afterwards, we ramped up the large spacing component ($a_{sl} = 2.3 \mu\text{m}$) of a superlattice [31, 32] in y -direction to prepare independent one-dimensional (1d) tubes. Next, we slowly turned on a lattice with spacing $a_l = 1.15 \mu\text{m}$ along the tubes in x -direction using a 100 ms linear ramp to $11 E_R$, where $E_R = \hbar^2/8ma_l^2$ denotes the recoil energy of the lattice for atoms of mass m . The hopping strength is $t = \hbar \times 125(9) \text{ Hz}$ at this final lattice depth. The lattice filling was controlled by varying the evaporation parameters. To simultaneously detect the spin and charge degrees of freedom of the 1d Hubbard chains locally, we froze the dynamics by rapidly increasing the lattice depth along the tubes to $42 E_R$ within 1 ms, followed by a turn-off of the magnetic offset field in 20 ms. Spin resolution was obtained using the superlattice potential and a magnetic field gradient in y -direction in a Stern-Gerlach like setting. The magnetic field gradient shifted the potential

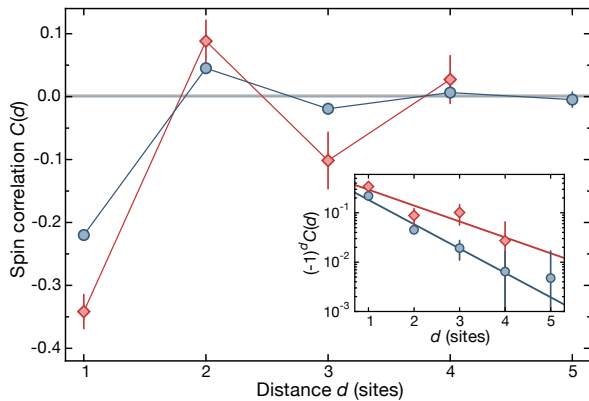


FIG. 2. **Antiferromagnetic spin correlations versus distance.** The main figure shows the measured spin correlations at $U/t = 12.6$ averaged over all sites with a density $\langle \hat{n}_i \rangle = 1 \pm 0.3$ in all tubes (blue). The staggered behavior directly visualizes the antiferromagnetic nature of the correlations $C(d)$. When filtering to the lowest entropy tube and analyzing only sites where the density is $\langle \hat{n}_i \rangle = 1 \pm 0.1$ we observe even stronger correlations (red). Correlations up to three sites are statistically significant. As a test for the 1d character of the system, we also show the transverse (inter tube) nearest neighbor correlations averaged over all measurements (gray line with one standard deviation of the mean (s.e.m.) uncertainty represented by the lighter area). The inset shows the decay of the rectified spin correlations $(-1)^d C(d)$ in a logarithmic plot together with an exponential fit $C(d) \propto \exp(-d/\xi)$, which reveals an average correlation length of $\xi = 0.9(1)$ sites and $\xi = 1.4(4)$ sites for the lowest entropy tube. All error bars represent one s.e.m.

minima experienced by the two spin states of opposite magnetic moment and the subsequent adiabatic ramp-up of the short scale component of the y -superlattice with well separation a_l caused a separation of the spins into the two different sites of the local double well (see Fig. 1a). Applying this technique to a spin polarized gas, we inferred a splitting fidelity of 98% limited by superlattice phase fluctuations of 25 mrad [30]. Finally, we ramped up a three-dimensional pinning lattice for detection and reconstructed the lattice site occupations from fluorescence images (see Fig. 1(b,c)), deconvolved with our measured point-spread-function [24, 30]. The above detection procedure enables us to detect the position of all spins, doublons and holes in the system with single lattice site resolution, thereby obtaining complete information about the system in Fock space.

First, we analyze the spin correlations $C(d) = 4(\langle \hat{S}_i^z \hat{S}_{i+d}^z \rangle - \langle \hat{S}_i^z \rangle \langle \hat{S}_{i+d}^z \rangle)$ between the spin operators $S_i^z = (\hat{n}_{i,\uparrow} - \hat{n}_{i,\downarrow})/2$ versus distance d . To this end, we fixed the s -wave scattering length to $671(10) a_B$, where a_B is the Bohr radius, corresponding to $U/t = 12.6$ and took a high statistics dataset of 1200 individual pictures. Our analysis involves all sites with an average density $\langle \hat{n}_i \rangle = \langle \hat{n}_{i,\uparrow} + \hat{n}_{i,\downarrow} \rangle$ in the range $\langle \hat{n}_i \rangle = 1 \pm 0.3$. Furthermore, we disregard some of the lattice sites, on which the

Stern-Gerlach based spin detection is biased due to lattice inhomogeneities [30]. The observed strong nearest-neighbor correlations of $C(1) = -0.220(5)$ correspond to 37% of the expected zero temperature signal in the Heisenberg limit [27, 28] (see Fig. 2). We observe significant correlations over a distance of up to three sites and a plot of the staggered correlator $C_s(d) = (-1)^d C(d)$ reveals the expected exponential decay at finite temperatures with a fitted decay length of $\xi = 0.9(1) a_l$. Our local resolved data allows for the selection of the lowest entropy, that is, the strongest correlated 1d system [30]. In the center of this tube we observed a nearest-neighbor correlation of $C(1) = -0.34(9)$ corresponding to 58% of the zero temperature prediction and a decay length of $\xi = 1.4(4) a_l$ when averaging over all measurements taken for $U/t > 8$ (cf. Fig. 3). This low entropy data is based on the statistical analysis of 1000 nearest neighbor and 760 next-nearest neighbor pairs. The measured values for the nearest and next-nearest neighbor correlations compare well with the strong coupling prediction of ref. [27]. Based on this comparison, we infer an entropy per particle of $s = 0.61(1)$ averaged over all tubes and $s = 0.49(4)$ in the center of the lowest entropy tube, significantly below $s^* = \ln(2) \approx 0.69$. The lowest entropy corresponds to a temperature of $T/t \lesssim 0.3$ at $U/t = 12.6$. Finally, we confirmed the absence of correlations between different tubes in y -direction, as expected for independent 1d systems.

In order to explore the properties of the Hubbard chains at different interaction strengths U/t , we measured spin correlations and particle-hole fluctuations for varying onsite interactions U , while keeping the lattice ramp and final lattice depth constant at $11 E_R$. The detailed dependence of the correlations on the interactions is expected to differ for isothermal and isentropic state preparation. In the former case, a maximum of the correlations is expected at intermediate interactions U/t , where part of the entropy is carried by charge modes [33]. In the latter case spin correlations saturate towards strong interactions, where the energetic gap between spin and charge modes is large. In Fig. 3, we show the evolution of the spin correlation for different distances together with the doublon and hole probabilities for different interactions. We observe a saturation behavior of the spin correlations for $U/t > 8$, most prominently visible for nearest-neighbors. Simultaneously, the doublon and hole fractions, reach their lowest value of $P_d = 5\%$ and $P_h = 12\%$. The higher hole fraction indicates a slight effective hole doping in the analyzed region of our system, which is lower ($P_d = 3\%$, $P_h = 7\%$) for the data contributing to the lowest entropy tube. Comparing the spin correlations along the Hubbard chains to the ones along the perpendicular direction stresses the statistical significance of the measured next-next-nearest neighbor signal ($d = 3$), since the uncorrelated reference is consistently above it for stronger interactions.

To obtain more insight into the behavior of the spin correlations, we make use of our full microscopic charac-

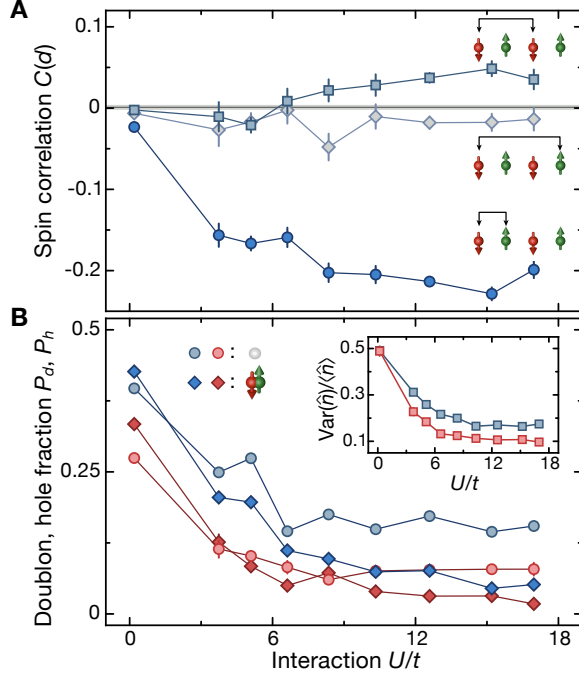


FIG. 3. **Spin and charge degrees of freedom at different interaction strength.** (A) Spin correlations $C(d)$ at different distances d versus interaction strength U/t . Starting from zero at vanishing interactions the finite range spin correlations develop and saturate for interaction strengths $U/t > 8$. This behavior indicates an adiabatic evolution of the system during lattice ramp up. The pictograms illustrate the range of the respective correlator (from $d = 1$ to $d = 3$). The gray line with surrounding lighter shading represents the transverse nearest neighbor correlations and its uncertainty. (B) Evolution of the charge degree of freedom. We show data for the less restrictive density filter, requiring $\langle\hat{n}_i\rangle = 1 \pm 0.3$ (blue), and for the lowest entropy line filtered to sites with $\langle\hat{n}_i\rangle = 1 \pm 0.1$ (red). The main figure shows the evolution of holes (circles) and doublons (diamonds) with interaction strength U/t , also illustrated by the pictograms. The hole (P_h) and doublon (P_d) fractions decrease for low interactions and then saturate. The higher hole fraction reveals a slight effective hole doping of the system due to the regions of lower density, which is significantly reduced for the stronger filtered data. The inset shows the evolution of the atom number fluctuations normalized to the mean density, $\text{Var}(\hat{n})/\langle\hat{n}\rangle$. The fluctuations are suppressed already at vanishing interactions due to effects of Pauli blocking in the metal. This suppression becomes stronger for increasing interactions until the fluctuations saturate. All error bars represent one s.e.m and the apparent fluctuation of the data is due to day-to-day systematics in our data.

terization of the system. To study the antiferromagnetic spin correlations away from half filling, we show the nearest neighbor correlator $C(1)$ per pair of sites versus their mean density in Fig. 4. This data combines different datasets taken at $U/t = 10.3$ and also contains measurements at different temperatures, obtained by holding the cloud for up to 2.5 s in the two-dimensional plane. We

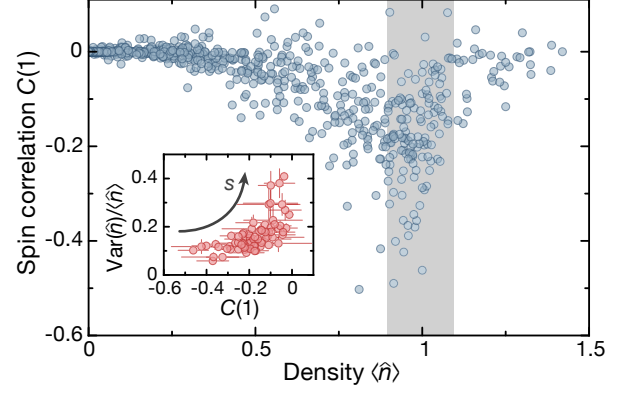


FIG. 4. **Nearest neighbor spin correlations versus density and fluctuations.** We show the nearest neighbor spin correlations $C(1)$ for different densities corresponding to different positions in the trap. The data combines several measurements at an interaction strength of $U/t = 10.3$, also including higher temperature data. The spin correlations $C(1)$ peak just below densities of one, consistent with the half filling regime taking our detection efficiency into account. In the inset we plot the normalized density fluctuations $\text{Var}(\hat{n})/\langle\hat{n}\rangle$ versus $C(1)$ for a density interval $\langle\hat{n}_i\rangle = 1 \pm 0.1$ as indicated by the gray area. Density fluctuations rise steeply for low values of the spin correlator signaling the saturation of the entropy in the spin sector. This characteristic dependence identifies the vertical scatter of the data in the main figure as a result of different local entropies s as indicated by the arrow. For clarity of the presentation we omit the error bars in the main figure, in the inset they correspond to one s.e.m.

observe a clear dependence of the spin correlator on the local density, peaking just below $\langle\hat{n}\rangle = 1$, where the deviation from one is consistent with a small loss of atoms during the detection [24]. Away from half filling, both to higher and lower densities, a strong decrease of the correlations is observed reflecting the fact that doping reduces spin order [2]. Generally, the data scatters strongly, that is, at a given density we observe events with a range of significantly different nearest neighbor spin correlations. This reflects the distribution of entropy within each cloud, as well as between the measurement settings. To further analyze the data, we selected a density interval $\langle\hat{n}_i\rangle = 1 \pm 0.1$ and calculated the density fluctuations $\text{Var}(\hat{n})/\langle\hat{n}\rangle$ for all sites with mean densities in this window. These density fluctuations reflect the entropy in the charge sector, while the nearest neighbor spin correlations are a measure of the spin entropy and we show their mutual dependence in the inset of Fig. 4, identifying two distinct regimes of total entropy. In the regime below $s^* = \ln(2)$ ($C(1) \lesssim 0.15$), the charge fluctuations are predicted to depend only weakly on the total entropy [27, 28], which in turn is stored in the spin fluctuations. Only when these are saturated at s^* , the density fluctuations grow, visible in the steep rise of the density fluctuations for spin correlations just below zero. This

freezing of charge fluctuations renders them useless as a thermometer in the low entropy regime, while spin correlations, on the other hand, are ideal for this purpose because they show a strong dependence on temperature (entropy) down to $T = 0$ [27].

In conclusion, we have reached the low entropy regime of one-dimensional Hubbard chains in which finite range antiferromagnetism starts to develop. The inferred entropy is consistently below the critical value of $\ln(2)$ reaching $s \approx 0.5$ in our lowest entropy 1d tube. Combining our quantum gas microscope with optical superlattices, we demonstrated the simultaneous detection of all relevant degrees of freedom. We characterized the state of the Hubbard chains at different interaction strength in terms of spin correlations and charge fluctuations. The measurable spin correlation signal extended over three sites, well beyond nearest-neighbors. Using a local analysis, we were able to present a first study of the behavior of the spin correlations away from half filling. The demonstrated ability to characterize spin correlations in 1d systems locally provides a useful thermometer in the low entropy regime where charge fluctuations are frozen [27, 28]

and cannot serve anymore as a thermometer. Such a “spin thermometer” [34] is a crucial step towards optimized cooling [35, 36] to even lower entropies. Furthermore, the combination of superlattices and local detection will allow for the search of an adiabatic path between low entropy valence bond solids [15] or plaquette RVB states [37, 38] and the Heisenberg antiferromagnet [39], also in two dimensions. Realization of the paradigmatic quantum phase transition from such an artificial valence bond solid to a Heisenberg antiferromagnet [40] thereby seem within reach of present experiments.

During the completion of this manuscript we became aware of similar experimental results in two dimensions [41].

ACKNOWLEDGEMENTS

We acknowledge help by K. Kleinlein and M. Lohse during the setup of the experiment and financial support by MPG and EU (UQUAM).

-
- [1] P. W. Anderson, *Science* **235**, 1196 (1987).
 - [2] K. L. Hur and T. M. Rice, *Annals of Physics* **324**, 1452 (2009).
 - [3] A. Auerbach, *Interacting Electrons and Quantum Magnetism* (Springer Science & Business Media, 1994).
 - [4] T. Giamarchi, *Quantum Physics in One Dimension* (Clarendon Press, 2004).
 - [5] T. Esslinger, *Annual Review of Condensed Matter Physics* **1**, 129 (2010).
 - [6] R. Jördens, N. Strohmaier, K. Günter, H. Moritz, and T. Esslinger, *Nature* **455**, 204 (2008).
 - [7] U. Schneider, L. Hackermüller, S. Will, T. Best, I. Bloch, T. A. Costi, R. W. Helmes, D. Rasch, and A. Rosch, *Science* **322**, 1520 (2008).
 - [8] R. Jördens, L. Tarruell, D. Greif, T. Uehlinger, N. Strohmaier, H. Moritz, T. Esslinger, L. De Leo, C. Kollath, A. Georges, V. Scarola, L. Pollet, E. Burovski, E. Kozik, and M. Troyer, *Physical Review Letters* **104**, 180401 (2010).
 - [9] S. Taie, R. Yamazaki, S. Sugawa, and Y. Takahashi, *Nature Physics* **8**, 825 (2012).
 - [10] P. M. Duarte, R. A. Hart, T.-L. Yang, X. Liu, T. Paiva, E. Khatami, R. T. Scalettar, N. Trivedi, and R. G. Hulet, *Physical Review Letters* **114**, 070403 (2015).
 - [11] D. Greif, M. F. Parsons, A. Mazurenko, C. S. Chiu, S. Blatt, F. Huber, G. Ji, and M. Greiner, *Science* **351**, 953 (2016).
 - [12] L. W. Cheuk, M. A. Nichols, K. R. Lawrence, M. Okan, H. Zhang, and M. W. Zwierlein, *arXiv:1604.00096* (2016).
 - [13] C. Hofrichter, L. Riegger, F. Scazza, M. Höfer, D. R. Fernandes, I. Bloch, and S. Fölling, *arXiv:1511.07287* (2015).
 - [14] E. Cocchi, L. A. Miller, J. H. Drewes, M. Koschorreck, D. Pertot, F. Brennecke, and M. Köhl, *Physical Review Letters* **116**, 175301 (2016).
 - [15] S. Trotzky, Y.-A. Chen, U. Schnorrberger, P. Cheinet, and I. Bloch, *Physical Review Letters* **105**, 265303 (2010).
 - [16] D. Greif, T. Uehlinger, G. Jotzu, L. Tarruell, and T. Esslinger, *Science* **340**, 1307 (2013).
 - [17] D. Greif, G. Jotzu, M. Messer, R. Desbuquois, and T. Esslinger, *Physical Review Letters* **115**, 260401 (2015).
 - [18] R. A. Hart, P. M. Duarte, T.-L. Yang, X. Liu, T. Paiva, E. Khatami, R. T. Scalettar, N. Trivedi, D. A. Huse, and R. G. Hulet, *Nature* **519**, 211 (2015).
 - [19] S. Murmann, F. Deuretzbacher, G. Zürn, J. Bjerlin, S. Reimann, L. Santos, T. Lompe, and S. Jochim, *Physical Review Letters* **115**, 215301 (2015).
 - [20] L. W. Cheuk, M. A. Nichols, M. Okan, T. Gersdorf, V. V. Ramasesh, W. S. Bakr, T. Lompe, and M. W. Zwierlein, *Physical Review Letters* **114**, 193001 (2015).
 - [21] M. F. Parsons, F. Huber, A. Mazurenko, C. S. Chiu, W. Setiawan, K. Wooley-Brown, S. Blatt, and M. Greiner, *Physical Review Letters* **114**, 213002 (2015).
 - [22] E. Haller, J. Hudson, A. Kelly, D. A. Cotta, B. Peaudecerf, G. D. Bruce, and S. Kuhr, *Nature Physics* **11**, 738 (2015).
 - [23] G. J. A. Edge, R. Anderson, D. Jervis, D. C. McKay, R. Day, S. Trotzky, and J. H. Thywissen, *Physical Review A* **92**, 063406 (2015).
 - [24] A. Omran, M. Boll, T. A. Hilker, K. Kleinlein, G. Salomon, I. Bloch, and C. Gross, *Physical Review Letters* **115**, 263001 (2015).
 - [25] G. Zürn, T. Lompe, A. Wenz, S. Jochim, P. Julienne, and J. Hutson, *Physical Review Letters* **110**, 135301 (2013).
 - [26] J. Sirker and A. Klümper, *Physical Review B* **66**, 245102 (2002).

- [27] E. V. Gorelik, D. Rost, T. Paiva, R. Scalettar, A. Klümper, and N. Blümer, *Physical Review A* **85**, 061602 (2012).
- [28] B. Sciolla, A. Tokuno, S. Uchino, P. Barmettler, T. Giamarchi, and C. Kollath, *Physical Review A* **88**, 063629 (2013).
- [29] F. H. L. Essler, H. Frahm, F. Göhmann, A. Klümper, and V. E. Korepin, *The One-Dimensional Hubbard Model* (Cambridge University Press, 2005).
- [30] See supporting material.
- [31] J. Sebby-Strabley, M. Anderlini, P. Jessen, and J. Porto, *Physical Review A* **73**, 033605 (2006).
- [32] S. Fölling, S. Trotzky, P. Cheinet, M. Feld, R. Saers, A. Widera, T. Müller, and I. Bloch, *Nature* **448**, 1029 (2007).
- [33] F. Werner, O. Parcollet, A. Georges, and S. R. Hassan, *Physical Review Letters* **95**, 056401 (2005).
- [34] R. Olf, F. Fang, G. E. Marti, A. MacRae, and D. M. Stamper-Kurn, *Nature Physics* **11**, 720 (2015).
- [35] J.-S. Bernier, C. Kollath, A. Georges, L. De Leo, F. Gerbier, C. Salomon, and M. Köhl, *Physical Review A* **79**, 061601 (2009).
- [36] T.-L. Ho and Q. Zhou, *Proceedings of the National Academy of Sciences* **106**, 6916 (2009).
- [37] S. Trebst, U. Schollwöck, M. Troyer, and P. Zoller, *Physical Review Letter* **96**, 250402 (2006).
- [38] S. Nascimbène, Y.-A. Chen, M. Atala, M. Aidelsburger, S. Trotzky, B. Paredes, and I. Bloch, *Physical Review Letters* **108**, 205301 (2012).
- [39] M. Lubasch, V. Murg, U. Schneider, J. I. Cirac, and M.-C. Bañuls, *Physical Review Letters* **107**, 165301 (2011).
- [40] T. Senthil, A. Vishwanath, L. Balents, S. Sachdev, and M. P. A. Fisher, *Science* **303**, 1490 (2004).
- [41] M. F. Parsons, A. Mazurenko, C. S. Chiu, G. Ji, D. Greif, and M. Greiner, arXiv: 1605.02704 (2016).
- [42] S. Trotzky, P. Cheinet, S. Fölling, M. Feld, U. Schnorrberger, A. M. Rey, A. Polkovnikov, E. A. Demler, M. D. Lukin, and I. Bloch, *Science* **319**, 295 (2008).
- [43] D. S. C. Biggs and M. Andrews, *Applied Optics* **36**, 1766 (1997).
- [44] E. L. Hazlett, Y. Zhang, R. W. Stites, and K. M. O'Hara, *Physical Review Letters* **108**, 045304 (2012).
- [45] H. P. Büchler, *Physical Review Letters* **104**, 090402 (2010).

SUPPORTING MATERIAL

I. CLOUD PREPARATION

Our experiments started with a degenerate, incoherent spin mixture of the lowest two hyperfine states of lithium-6 in a single two-dimensional plane of a vertical lattice with spacing $a_z = 3.1 \mu\text{m}$ and depth of $V_z = 185 E_R$. The resulting harmonic confinement in z -direction was $\omega_z = 2\pi \times 22.5 \text{ kHz}$. Distinct to prior experiments [24], this single plane was directly loaded from a strongly elliptical shaped dimple trap propagating in y -direction with beam waists $w_x = 10.3 \mu\text{m}$ and $w_z = 1.7 \mu\text{m}$ in x - and z -direction, respectively, at a magnetic field of 599 G corresponding to a scattering length $a_s = 353 a_B$. A further crossed dipole trap beam propagating along

the z -direction ($w_{xy} = 75 \mu\text{m}$) was used to provide additional radial confinement in the two-dimensional plane. The final evaporation was performed in the single lattice plane with the additional cross trap by ramping up a magnetic field gradient along the y -direction in 2.5 s to 25 G/cm. After ramping down the magnetic field gradient, we set the scattering length value (and thus the final interaction strength U in the lattice) by varying the homogeneous magnetic field between 529 G and 657 G. We adjusted the peak density of the two dimensional gas to approximately $1/(1.15 \times 2.3) \mu\text{m}^{-2}$, the required density for unity lattice occupation, by lowering the power of the cross trap beam. To prepare one dimensional tubes, we linearly ramped up the long scale component of a superlattice in y -direction ($a_{sl} = 2.3 \mu\text{m}$) to a depth of $34 E_R$ in 100 ms. The remaining tunnel coupling between the tubes is below one Hertz and negligible on the timescales studied here, yielding decoupled and independent tubes. Subsequently, we ramped up a short scale lattice ($a_l = 1.15 \mu\text{m}$) along the tubes in x -direction in 100 ms to a lattice depth of $11.0(4) E_R$, which results in a tunnel coupling of $t = \hbar \times 125(9) \text{ Hz}$. The lattice depths in x, y, z -direction are given in units of the respective recoil energies: $E_R = \hbar \times 6.28 \text{ kHz}$, $\hbar \times 1.57 \text{ kHz}$, $\hbar \times 0.87 \text{ kHz}$.

II. DETECTION

A. Spin resolved detection

The detection sequence was initiated by freezing out the dynamics along the tubes with an abrupt (1 ms) increase of the lattice depths to $42 E_R$, $84 E_R$ and $278 E_R$ in the x -, y - and z -direction. Then, we ramped down the magnetic Feshbach field to 1 G to enter the Zeeman regime, where both spin components have equal and opposite magnetic moments. To directly probe both the local population and the spin state, we used the short scale component of the superlattice in y -direction in combination with a magnetic field gradient [42]. Here, the full superlattice potential is described by

$$V = V_l \cos^2(k_l y + \varphi) + V_{sl} \cos^2\left(\frac{k_l}{2} y\right), \quad (2)$$

with lattice depths $V_{l,sl}$ and wave vector $k_l = \pi/a_l$. The relative phase of the superlattice φ controlling its symmetry was set such that the local double wells were symmetric. This was verified by measuring the double well imbalance versus superlattice phase φ for a spin polarized sample as shown in Fig. 5. The magnetic field gradient was first set to 60(5) G/cm before adiabatically ramping up the short scale superlattice component with spacing $a_l = a_{sl}/2$ to $V_l = 17 E_R$ in 10 ms while ramping down the long scale component to $V_{sl} = 10 E_R$. The corresponding energy offset due to the Zeeman shift between the left and the right lattice wells was $\Delta E_{LR} = \pm \hbar \times 6.2(6) \text{ kHz}$

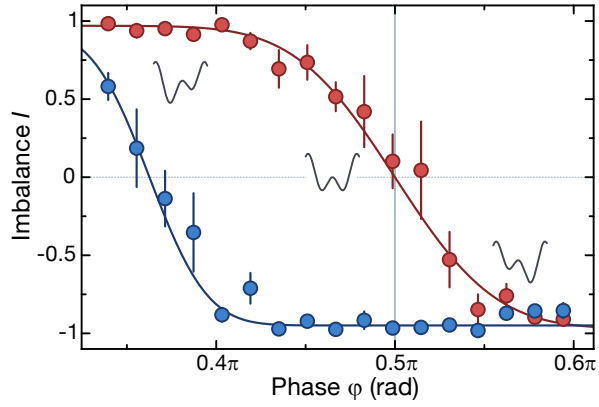


FIG. 5. **Spin selective imaging via deterministic splitting in local double wells.** The figure shows the local atom number imbalance $I = (n_{\text{left}} - n_{\text{right}})/(n_{\text{left}} + n_{\text{right}})$ in the local double wells for the central region of the cloud versus the superlattice phase φ . This externally controlled phase φ sets the symmetry of the double wells. For this measurement a spin polarized sample was used, of which the preparation is described in ref. [24]. The red data was taken without, the blue data with the magnetic gradient field of 60(5) G/cm, and the solid lines are error function fits to the data. The splitting was done at the symmetric point ($\varphi = \pi/2$) of the superlattice potential, where the gradient-free measurement showed zero imbalance (gray line). Taking into account our detection fidelity of 95%, the splitting fidelity of 98% is estimated from the value of the imbalance in presence of the magnetic field gradient at $\varphi = \pi/2$. Error bars denote one s.e.m.

for the spin up and down value respectively. As a result of their opposite magnetic moments, the spin components were adiabatically transferred into different sites of the local double well in a deterministic way and measuring their positions gave access to their spin state. This sequence ensured a spin separation fidelity of 0.98 (see Fig 5). For the magnetic field gradient of 60(5) G/cm, we estimated that the relative phase $\varphi = \pi/2$ between the short and long scale components of the superlattice had to be controlled to better than 100 mrad, which we extracted from the width of the red curve of Fig 5 obtained without applying any magnetic field gradient. The shot-to-shot rms-fluctuation of the phase was measured to be 25 mrad by direct imaging of the superlattice potential after the chamber.

B. Reconstruction of the site occupation

Compared to our previous publication [24], we improved our population reconstruction algorithm. In this work, we used an accelerated Richardson-Lucy deconvolution [43] with a measured point-spread-function that we obtained by averaging the image of 1000 isolated atoms. The resulting deconvolved image after 100 steps of the Richardson-Lucy algorithm contained the signal for ev-

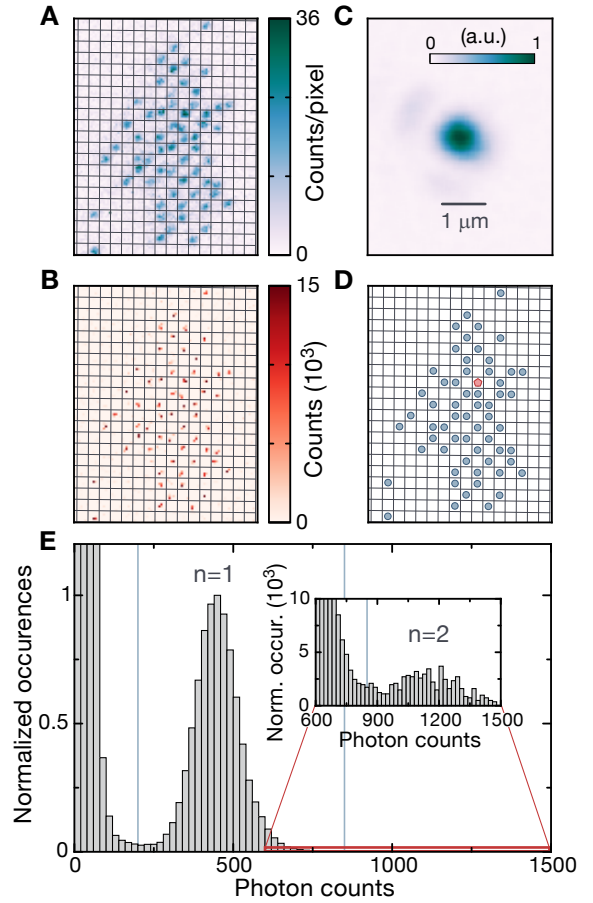


FIG. 6. **Reconstruction of the lattice occupation.** (A) Typical raw fluorescence image with overlaid lattice grid. The color scale gives the photon counts per pixel of the CCD camera. (B) Point-spread-function of the imaging system with color scale in relative units. The Gaussian widths are $\sigma_1 = 314$ nm and $\sigma_2 = 363$ nm along the principal axes. (C) Deconvolved image from (A) using the point-spread-function shown in (B) using a Richardson-Lucy deconvolution algorithm [43]. The color scale represents the counts per pixel after this deconvolution. (D) Reconstructed lattice site occupation showing empty sites, singly occupied ones (blue) and one doublon (red). (E) Histogram of photon counts per site. The separation between empty and singly occupied sites is excellent, with the counts in the intermediate region dominated by hopping events. The inset is a zoom into the region indicated by the red box revealing the doublon peak, which is clearly visible even for the very low number of detected doublons after magnetic splitting ($< 1\%$). We indicate the boundaries for identifying one and two atoms per site by the vertical lines.

ery atom almost on a single pixel (see Fig. 6). Integration of the counts in the region of each lattices site allowed us to identify sites with zero, one and two atoms with high fidelity thanks to our parity-free detection [24]. We obtained a fidelity of $> 99\%$ for distinguishing zero and one, and a fidelity of $> 95\%$ for distinguishing one and two atoms per site. Doubly occupied sites after spin splitting

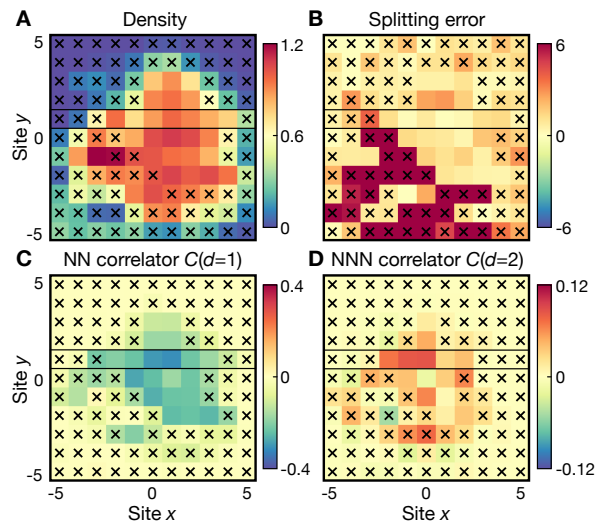


FIG. 7. **Selection of the relevant lattice sites used in the statistical analysis.** We define the region of interest for the statistical analysis based on the local density and the mean imbalance after spin splitting as described in the main text. The figure shows four different local observables for the $U/t = 12.6$ dataset. Sites marked with an “x” are discarded due to the density or imbalance filter and the black box marks the lowest entropy line. **(A)** Density $\langle \hat{n}_i \rangle$ per lattice site. We took only sites with $\langle \hat{n}_i \rangle = 1 \pm 0.3$ into account, with a more restrictive filter of $\langle \hat{n}_i \rangle = 1 \pm 0.1$ for the results quoted for the lowest entropy line. **(B)** Splitting error in the spin resolved detection due to interference structures in the lattice beams. Shown is the splitting error, that is, the mean detected spin imbalance per site after splitting, normalized to the root-mean-squared uncertainty of the mean of a binomial distribution. We took only sites into account on which the splitting error was below 3.5. **(C)** Local measurement of the nearest neighbor spin correlator $C(d=1)$. **(D)** Local measurement of the next-nearest neighbor spin correlator $C(d=2)$. In (C) and (D) we draw the spin correlation only on the left partner of each pairs.

arise from atoms in higher band, non perfect splitting and tunneling during the exposure. We detected less than 0.5 of these events per image for the measurements reported here.

C. Definition of the region of interest

To define the region of interest on which we evaluate the data, we use the mean occupation and the mean spin imbalance per site. For the occupation, we took all sites with $0.7 < \langle \hat{n}_i \rangle < 1.3$, effectively restricting the analysis region to the center of the cloud. The chain with lowest entropy quoted in the main text was selected based on the highest nearest-neighbor spin correlations signal averaged over all data sets taken for interactions $U/t > 8$, for which we observed saturation of the spin correlations. Also, we further restricted the analysis to the center of this line by requiring a mean density of $0.9 < \langle \hat{n}_i \rangle < 1.1$.

A second filter is required due to short-scale imperfections in our lattice potentials. These are due to interference fringes in the projected lattice beams, which we minimized but not removed entirely. These fringes spoil the symmetry of the superlattice double wells locally, leading to a slightly biased splitting of the two spins. To remove this effect from our data, we took into account only sites on which we detected a small enough spin imbalance (see Fig. 7). Our precise superlattice phase control ensured a typical mean imbalance of $I = 0.008(6)$. We filter sites that are incompatible with a splitting imbalance of less than $I = 0.05$ on a 3.5σ level. The position of the fringes drifts slowly on the timescale of days and we select the relevant sites per dataset, typically measured over several hours. The local occupation, imbalance and extracted spin correlators are shown in Fig. 7 for the dataset measured at $U/t = 12.6$.

III. CALIBRATION OF HUBBARD PARAMETERS

A. Lattice depth and tunneling calibration

The generation of the lattice potentials via projection through the objective is described in our previous work [24]. We calibrated the depth of the various lattices via lattice modulation spectroscopy. To this end, we used a spin polarized sample in the $|1\rangle = |F=1/2, m_F=-1/2\rangle$ state. After the lattice was ramped to the desired value, we modulated its intensity for 300 ms with an amplitude of $\pm 3\%$. We measured the number of transferred atoms from the ground to the second excited band versus the modulation frequency by counting the number of holes. Finally, the tunneling rates were estimated from a band structure calculation for our measured lattice depths.

B. Calibration of the interaction strength

The calibration of the interaction strength is based on the magnetic field tuned s -wave scattering length a_s , which has been precisely characterized [25]. The required magnetic field calibration was done by locating the narrow Feshbach resonance at 543.286 G [44] via its associated atom loss feature in a spin balanced sample, which allowed for a calibration of the magnetic field to 0.2 G. The onsite interaction U was then calculated using the Wannier function of the lowest band for our measured lattice depths. Because of the large lattice spacing, we expect only small corrections to the interaction strength due to multi-band effects [45]. Even at the largest scattering length $a_s = 904 a_B$ used in this manuscript, the ratio to the shortest lattice spacing is only $a_s/a_l = 0.04$. In Table S1 we summarize the relevant values of the magnetic field, the scattering length and the calculated interaction strength.

Magnetic field (G)	Scattering length (a_B)	Onsite inter- action U/h (Hz)	U/t
529	8	19	0.1
573	200	463	3.7
586	272	630	5.1
598	353	820	6.6
611	445	1034	8.4
624	550	1279	10.3
637	671	1560	12.6
649	810	1883	15.2
657	904	2101	17.0

TABLE I. Summary of the interaction parameters used in our measurements.